Development of a predictive capability of short-pulse laser-driven broadband x-ray radiography

Hiroshi Sawada[1], Christopher M. Salinas[1], Farhat N. Beg[2], Hui Chen[3], Anthony J. Link[3], Harry S. McLean[3], Pravesh K. Patel[3], Yuan Ping[3] and Gerald J. Williams[3]

[1] Department of Physics, University of Nevada Reno, Reno, Nevada, 89557-0220, U.S.A.
[2] University of California San Diego, La Jolla, CA, 92093, USA
[3] Lawrence Livermore National Laboratory, Livermore, CA, 94550, USA

E-mail: hsawada@unr.edu

Received xxxxxx
Accepted for publication xxxxxx
Published xxxxxx

Abstract

High intensity, short-pulse laser interaction with a solid metal target produces broadband hard x rays potentially for various applications of x-ray radiography. Here experimental benchmarking of numerical modelling for short-pulse laser-driven broadband x-ray radiography is presented. Angular dependent x-ray spectra are first calculated with a hybrid particle-in-cell code, Large Scale Plasma (LSP), using fast electron parameters inferred from an analysis of measured bremsstrahlung signals. Subsequently, an x-ray spectrum in the direction of radiography is used in photon transport calculations using a Monte Carlo code, Particle and Heavy Ion Transport code System (PHITS), to simulate a radiographic image including a modelled 3D test object, an x-ray attenuation filter and an image plate detector. Simulated radiographic images are compared with measurements obtained in an experiment using a 50-TW Leopard short-pulse laser at the University of Nevada Reno. Results show that simulations reproduce the experimental images well for three different attenuation filters (plastic, aluminium, and brass), while one-dimensional transmission profiles for the plastic and aluminium filters are quantitatively in good agreement. The modelling approach established in this work could be used as a predictive tool to simulate radiographic images of complex 3D solid objects at any arbitrary angular position or to optimize experimental components such as the source spectrum, x-ray attenuation filters and a detector type depending on a radiographic object without carrying out experiments.

Keywords: broadband x-ray radiography, short-pulse laser-produced x rays, hybrid particle-in-cell, Monte Carlo simulations

1. Introduction

High energy x rays produced by intense short-pulse lasers interacting with a solid has been studied for a broad range of applications such as basic plasma science [1], medical imaging [2,3], industrial and national security applications [4 , 5 , 6]. A large number of energetic (fast) electrons accelerated by the laser at a peak intensity greater than the relativistic intensity (> ~10^{18} W/cm^2) produces bremsstrahlung and characteristic x rays as the electrons propagate through the solid target. In inertial confinement fusion (ICF) experiments, such x-ray sources have been used to diagnose a high-density, compressed core through Kα radiography [7 , 8 , 9 , 10] or point-projection broadband radiography [11,12]. In particular, high-energy broadband x-ray spectra are essential to probe high density or high areal density objects such as strongly emitting dense ICF cores or millimetre-scale objects [4,13]. The diverging x-ray sources from the laser-solid interaction are suitable for recording radiographic images of large solid objects and/or multiple objects at different angular detector positions on a single shot.

A challenge for characterizing angular dependent broadband x rays from solids stems from lack of understanding of fast electron characteristics. Conventionally, modelling of fast electron and resulting x-ray generation with a short pulse laser has been performed using particle-in-cell (PIC), Monte Carlo (MC) or hybrid-PIC codes. [14,15] PIC codes calculate generation of fast electrons by solving the interaction of a high intensity laser pulse with a target. The fast electron information is then used either in the same PIC code [16] or handed over to MC/Hybrid-PIC codes [17] for photon generation calculations. Because of fine mesh sizes required to resolve the laser wavelength in PIC calculations, the codes do not fully simulate electron recirculation [18] that lasts significantly longer than the laser pulse duration. On the other hand, MC and Hybrid-PIC codes compute x-ray production by injecting a beam of fast electrons as a free parameter. An input electron spectrum for such simulations is chosen based on scaling laws [19,20,21], results of PIC calculations [17] or a parameter study by fitting experimental measurements [13,22]. Up to date, numerous experimental and numerical studies on characterization of laser-produced broadband x rays [23,24,25,26,27,28,29,30,31,32] are reported. Modelling of broadband x-ray spectrum has shown a reasonable agreement with experiments along a single line of sight, but a poor agreement in angular x-ray spectra produced particularly in a standalone foil. Recently, Daykin *et al.* report successful fast electron characterization by simultaneously matching angularly resolved bremsstrahlung measurements with hybrid PIC simulations. [33, 34] The modelling is performed by taking into account development of electric sheath potentials causing electron recirculation and an incident electron injection angle in a 2D Cartesian coordinate. On laser-based x-ray radiography, experimental radiographic images obtained using the laser-produced broadband sources are reported in several publications. [5,6,11,12, 35 , 36 , 37 , 38 , 39] However, no quantitative comparison between experimental and simulated images has been demonstrated.

In this paper, we present experimental benchmarking of numerical modelling for fast electron and x-ray source characterization as well as broadband x-ray radiography. Similar to the Daykin's approach, angular dependent broadband x-ray spectra are determined by fitting measured bremsstrahlung signals with a 2D hybrid PIC code, Large Scale Plasma (LSP) [40]. A calculated x-ray spectrum from

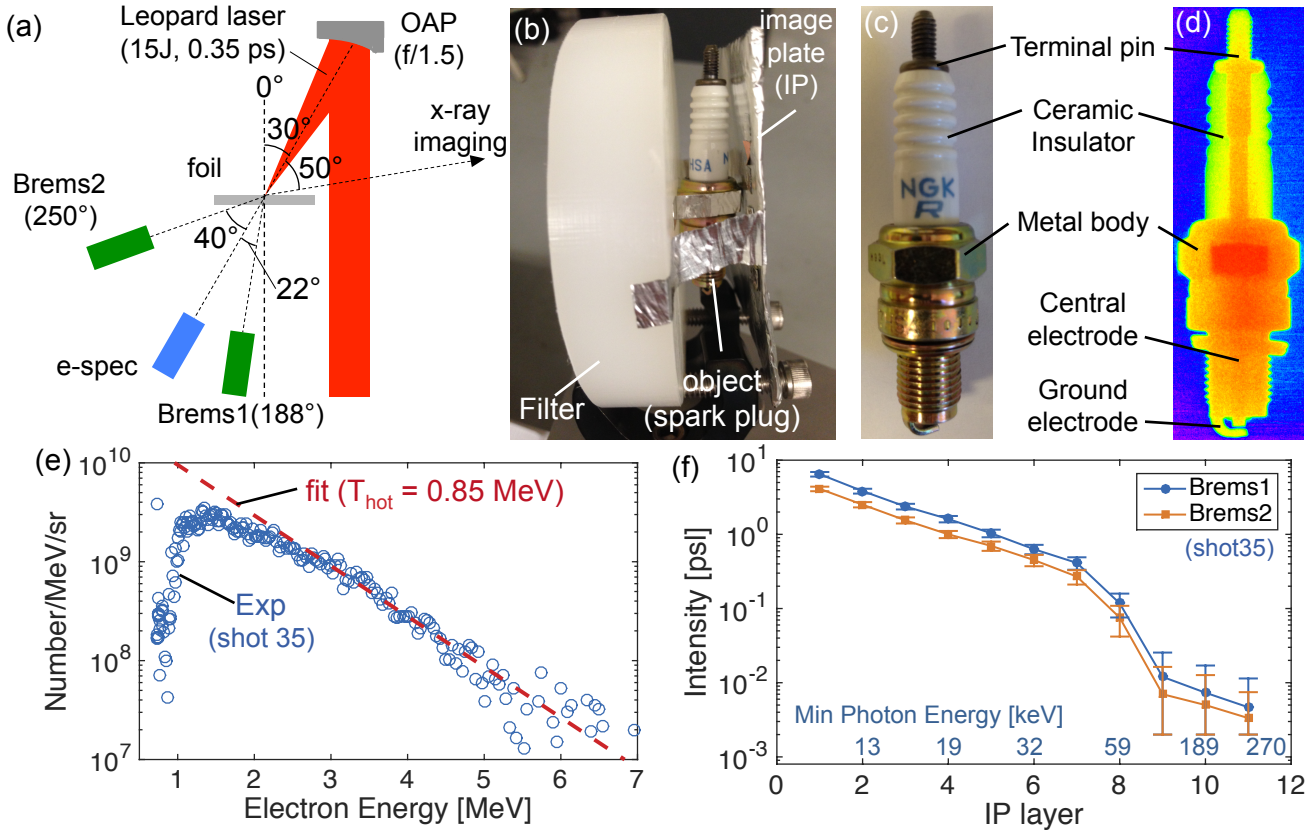

Figure 1 (a) A schematic of a Leopard laser experiment (top view). (b) A photograph of an x-ray radiographic package of a test object (spark plug), filter and IP. (c) A photograph and (d) x-ray radiographic image of the spark plug. (e) A measured electron spectrum. (f) Measured bremsstrahlung signals at Brems1 and Brems2.

LSP in the direction of a spark plug test object is used in a MC code, Particle and Heavy Ion Transport code System (PHITS) [41] to simulate a radiographic image. The widely used MC code together with an interactive three dimensional solid modelar, SimpleGeo [42], enables ones to straightforwardly incorporate a three dimensional complex object with real dimensions, exact compositions of filters and detectors that are necessary to calculate their photon sensitivities in transport calculations. It is noted that MC codes treat objects to be non-ionized matter (i.e., cold and solid density). Modelling of radiography for plasmas requires a radiative transfer code that calculates temperature- and density-dependent attenuation coefficients of the plasma. Simulated x-ray images and 1D transmission profiles are compared with measurements for three different filter materials (plastic, aluminium or brass).

2. Experiment

An experiment for x-ray source characterization and broadband x-ray radiography was carried out using a 50-TW Leopard short-pulse laser [43] at the University of Nevada Reno's Nevada Terawatt Facility. Figure 1(a) shows a schematic of the experiment. A metal planar foil (nominally 50~100 μm thick × 1000 μm^2 surface area) was irradiated by the laser with ~15 J energy in a 0.35 ps (FWHM) Gaussian pulse duration. The beam was tightly focused with an f/1.5 dielectric-coated off-axis parabolic mirror onto the target at an incident angle of 30° with an S-polarization. The peak intensity of the beam was estimated to be ~2×10^{19} W/cm^2 from a measured beam spot containing 30% of the energy within a 8 μm diameter. [44] The pedestal prior to the main pulse was measured with fast photodiodes to be of the order of 10^8 in intensity and ~1 ns long. [44]

Radiographic images of a spark plug (NGK CR7HSA [45]) were recorded in a point-projection geometry with a BAS-MS type image plate (IP) detector placed behind an x-ray attenuation filter and the test object as shown in Fig. 1(b). Major parts of the spark plug identified in the x-ray image in Fig. 1(d) are a terminal pin made of Fe, a ceramic insulator (Al_2O_3) and a metal body (stainless steel). The IP, spark plug and filter were packaged and positioned in the direction at 80° from the foil normal or near edge-on imaging geometry where the x-ray source size is restricted within the foil thickness. Since the entire foil emits x rays due to electron recirculation, the effective source size in the radiography direction is the projection of the 1000 μm^2 foil surface, which is estimated to be 173 μm [1000 μm ×sin(10°)] in the horizontal direction and 1000 μm in the vertical direction.

For fast electron characterization, bremsstrahlung x rays were measured with two differential filter stack spectrometers for a spectral range from 10 to 800 keV [46] at 22° and 40° from the laser axis, while fast electrons escaping from the target rear were measured with an absolutely calibrated magnet-based electron spectrometer [47] along the laser axis. Figure 1(e) and (f) show measurements of bremsstrahlung and escaping fast electrons for a 50 μm thick Cu foil. The bremsstrahlung and electron spectrometers were positioned at a distance of 48 cm and 27 cm from the target, respectively. A mean energy of the electrons characterized with an exponential slope known as a slope temperature is 0.85 ± 0.15 MeV. This is critical information indicating shot-to-shot variations in the laser-target interaction including changes in on-target laser and prepulse intensities. [48] The electron measurement is also used to confirm fast electron parameters estimated from a bremsstrahlung analysis described below because the escaped fast electrons are responsible for producing the bremsstrahlung. [49] Modeling of the bremsstrahlung and comparisons are briefly described in the next section and more details can be found in elsewhere [33, 34].

Main experimental variables were x-ray attenuation filters. Table 1 summarizes target types, experimental electron slope temperature and inferred fast electron parameters (simulated fast electron spectrum, T_{hot}, and divergence angle, θ) for three filter types (CH, Al and Brass). The thickness and material of the filters were a 19.1 mm thick plastic (polyethylene, C_2H_4, ρ=0.95 g/cm^3), 6.4 mm thick aluminium (ρ=2.70 g/cm^3) and 12.7 mm thick Brass [360 Brass alloy, Cu 61.5% Fe 0.35% Pb 2.5% Zn 35.4% by weight percent, ρ=8.50 g/cm^3]. Several different target types used in the experiment include various thicknesses of Al, Cu, Ag foils (50 ~ 300 μm thickness) and foils glued on a 6.35 mm thick (0.25 inches) plastic backing to prevent electron recirculation [50]. It is found that both electron slope temperatures and

Table 1 Summary of target shots studied for three x-ray attenuation filter materials. The experimental slope temperature is estimated from the fast electron measurements. The inferred fast electron parameters are from LSP modelling matching the bremsstrahlung measurements.

Shot	Filter type	Target type	Laser Energy [J]	Experimental slope temperature [MeV]	Inferred T_{hot} from LSP [MeV]	Inferred θ from LSP [°]
S34	CH (19.1 mm)	100μm Ag on a plastic backing	13.5	1.45 ±0.60	1.04 ±0.16	11.0 ±6.0
S35	Al (6.4 mm)	50μm Cu	10.0	0.85 ±0.15	0.87 ±0.17	10.5 ±5.5
S32	Brass (12.7 mm)	100μm Cu on a plastic backing	14.8	1.20 ± 0.35	0.98 ± 0.22	11.0 ± 6.0

divergence angles inferred from the bremsstrahlung analysis are similar regardless of the choices of the target types at the maximum laser energy. However, an appropriate selection of the target material is still necessary to calculate characteristic line emissions because Kα lines could strongly affect a transmission profile in a millimetre-scale object. [13] In the present case, contribution of line emissions to overall transmission is negligible in the cm-scale object.

3. Hybrid Particle-in-cell simulations using LSP

The measured bremsstrahlung spectra at the two angular positions were simultaneously fit by using a hybrid PIC code LSP to determine fast electron characteristics. In LSP, Kα and bremsstrahlung generation are calculated using the Integrated Tiger Series (ITS) code [51] as fast electrons propagate in the target. The simulations are performed in a 2D Cartesian coordinate system by injecting fast electrons at an incident angle of the laser beam and no laser-plasma interaction is solved. Calculations of electron stopping and angular bremsstrahlung with LSP are benchmarked against a MC code. [33] Note that a 2D Cylindrical simulation is unable to reproduce the difference in the experimental bremsstrahlung signals shown in Fig. 1(f), suggesting that the beam injection angle as well as relative detector positions with respect to the beam axis must be considered in fast electron transport and x-ray generation calculations.

Figure 2(a) shows a LSP simulation geometry for a 50 × 1000 μm^2 thick Cu foil. The colour contour in the figure represents the number of photons in the photon energies between 50 keV and 100 keV in a log scale. A beam of fast electrons is injected at an incident angle of 30° within a 20 μm plane at the foil surface (X=Z=0). The initial beam size is estimated based on an assumption that an electron beam is generated within the laser spot (~8 μm) at the critical density surface, which is 18 μm away from the solid surface according to a 1D hydrodynamics code [44]. It is noted that a choice of the initial beam spot size is insensitive to calculated angular distributions of x-ray spectra because of strong electron recirculation as seen in Fig. 2(a). The simulation box size is 1.6 mm x 1.6 mm with a cell size of 2 μm in each dimension for bare foils. All simulations are run up to 30 ps because photons between 50 and 100 keV are no longer produced at this time. The time step is determined in the code by using a Courant multiplier of 0.5.

Simulation parameters varied are: slope temperature of the fast electron energy spectrum (T_{hot}) and electron injection half-angle (θ). Changes in total injected energy only vary the total electron number so that simulated x-ray spectra simply scale with the energy in the simulation regime considered for

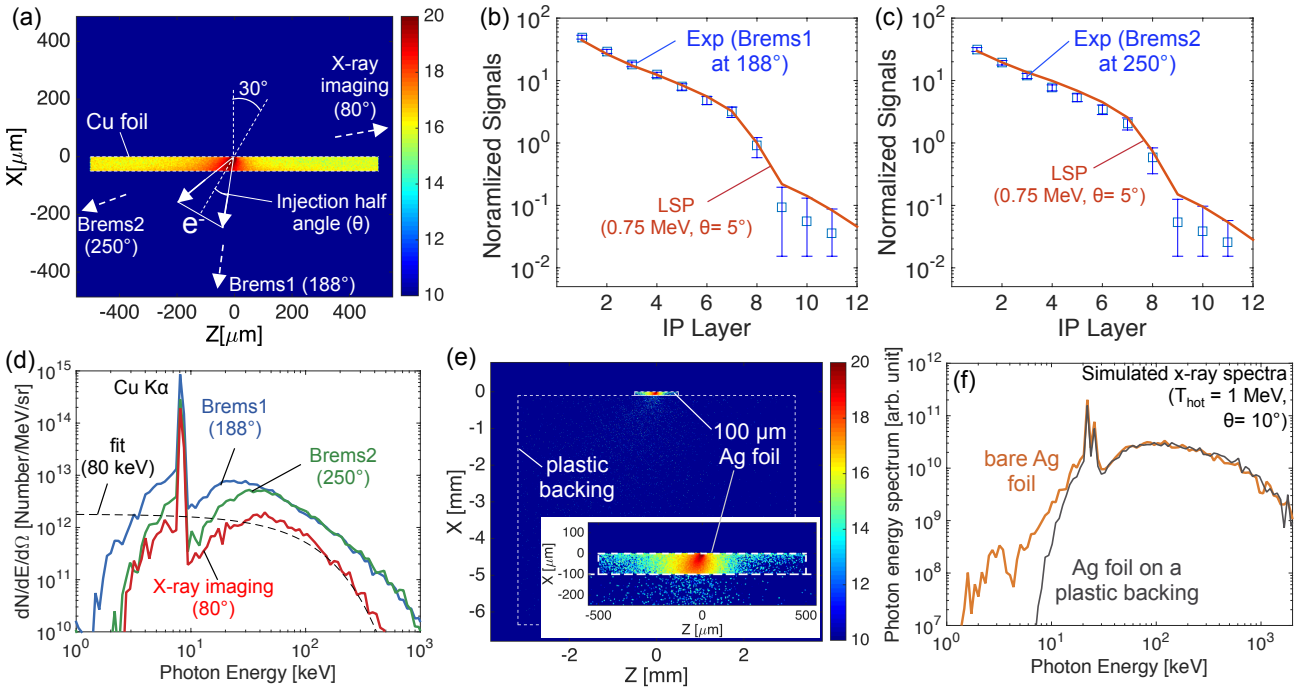

Figure 2 (a) A two dimensional photon generation distribution calculated with LSP for a 50 μm thick Cu foil. The colour contour represents the number of photons between 50 and 100 keV in a log scale. Comparisons of measured and calculated bremsstrahlung spectrometer signals for (b) Brems1 at 188° and (c) Brems2 at 250°. (d) Calculated x-ray spectra in the direction of Brems1, Brems2 and x-ray imaging. (e) A 2D LSP photon distribution for a 100um thick Ag foil with a plastic backing. The inset of the figure shows a close-up of the photon distribution near the Ag foil. (f) Calculated x-ray spectra for the Ag foil with and without the plastic backing.

this experiment (i.e., ~15 J laser energy). Dependence of the injected energy on the spectrum intensity, therefore, is cancelled out when the simulated spectrometer signals are normalized for comparing to measurements. More details of the fitting procedures, conversion from simulated x-ray spectra to spectrometer signals, and dependence of each parameter on simulated spectra are discussed in Refs 33 and 34.

The two bremsstrahlung signals are simultaneously fit with a series of LSP simulations by varying T_{hot} and θ in the range of $0.50 \le T_{hot} \le 1.50$ MeV and $5.0° \le \theta \le 30.0°$. A best fit is found to be $T_{hot} = 0.75$ MeV and $\theta = 5.0°$ in the range of $0.70 \le T_{hot} \le 1.03$ MeV and $5.0° \le \theta \le 10.5°$ from a reduced χ^2 analysis within 2 times the minimum χ^2 value. Fig. 2(b) and (c) show comparisons of the measured bremsstrahlung with calculations using $T_{hot} = 0.75$ MeV and $\theta = 5°$. The electron energy spectrum inferred from the fit agrees with the slope temperature observed in the direct electron measurement as shown in Table 1. Fig. 2(d) show calculated x-ray spectra using the electron parameters inferred in the direction of Brems1 (188°), Brems2 (255°) and the x-ray radiograph package (80°) for the 50 μm Cu target. The x-ray spectra in the direction of the bremsstrahlung spectrometers are similar above ~70 keV, but the spectrum at 80° is a factor of ~3 lower than the others. The continuous spectrum can be fit to a 80 keV exponential function. Strong angular dependence of the x-ray spectra from a solid implies that the characteristics of the x-ray source along the injection axis are high photon numbers and high photon energies, while the contribution of the bremsstrahlung in the total spectrum becomes smaller in the near edge-on direction.

For simulations of a metal foil glued on a plastic backing, the simulation box size is extended from 1.6 x 1.6 mm^2 to 8.0 x 8.0 mm^2. Fig. 2(e) displays a simulation setup for a 100 μm thick Ag foil attached on a 6350 $μm^2$ plastic layer. The colour contour in Fig. 2(e) and the inset illustrates time-integrated photon number distribution between 50 and 100 keV. A beam of injected fast electrons propagates through the Ag foil and the plastic layer without recirculating at the foil-plastic interface. As shown in Fig. 2(e), the majority of 50-100 keV photons is produced in the Ag foil since the production of bremsstrahlung is proportional to the square of the target atomic number (Z^2) [52] No development of a sheath potential is found at the rear surface of the Ag foil, but potentials developed at the other edges of the Ag foil. Because of the front surface recirculation, generation of x-ray photons is extended to almost the entire foil similar to the case of the bare foil. This creates a similar situation where the x-ray source size for the Ag-plastic target can be assumed to be similar to the bare foil case.

Fig. 2(f) compares calculated x-ray spectra with and without a plastic layer. The addition of the plastic to the metal foil significantly reduces x rays between 1 and ~ 30 keV including the 22 keV Ag Kα and 28 keV Kβ by ~30%. However, high-energy bremsstrahlung spectra (> ~50 keV) are nearly identical. This result is consistent with previous studies [6,50]. Effects of the electron recirculation on fast electron characteristics, particularly conversion efficiency, are an on-going research topic and beyond the scope of the present paper because simulated and experimental radiographic images are time-integrated and compared in a normalized unit (i.e., transmission). Currently, 3D LSP simulations are underway to determine conversion efficiencies from the laser to the fast electrons and resulting x rays. Results will be reported in a separate publication.

Similar parameter studies are performed for shot 34 (100 μm thick Ag on a plastic) and shot 32 (100 μm thick Cu on a plastic) to determine x-ray source spectrum. Fast electron parameters best fit to the measurements are $T_{hot} = 1.04 \pm 0.16$ MeV and $\theta = 11.0° \pm 6.0°$, and $T_{hot} = 0.98 \pm 0.22$ MeV and $\theta = 11.0° \pm 6.0°$ for shot 34 and 32, respectively. The inferred parameters summarized in Table 1 show that the fast electron spectra and divergence angles are relatively independent on the target materials, thicknesses and the absence of recirculation by adding the plastic backing at the similar peak laser intensity in this experiment.

4. Monte Carlo simulations with PHITS

X-ray radiographic images of the spark plug through the various filters are simulated with a Monte Carlo code, the

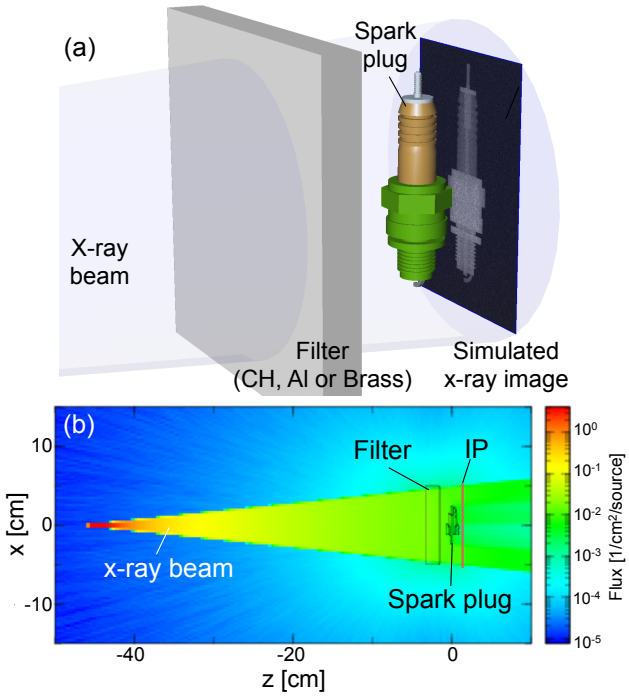

Figure 3 (a) A three dimensional model of a spark plug with a simulated x-ray image. (b) A PHITS simulation geometry in the x-z plane.

Particle and Heavy Ion Transport code System (PHITS), version 3.02 [41] using the LSP-calculated broadband spectrum. Figure 3(a) shows a spark plug model constructed with an interactive three-dimensional solid modelar, SimpleGeo [42]. The nominal material composition of the specific spark plug used is found in publicly available information [53 , 54]. The spatial dimensions of the simulation match the experiment. Figure 3(b) shows the x-z plane of a 3D PHITS simulation. The spark plug is positioned at the origin of the simulation space. A beam of photons spatially distributed over a plane of 173 × 1000 μm^2 is injected at z=-45.7 cm with a divergence of 6°. The photon energy distribution is implemented from the LSP simulation results for shots with each filter. The back surface of the filter and the front surface of the IP is positioned at z=-1.5 and 1.5 cm, respectively. The magnification of the imaging is approximately 1. The simulations are performed by injecting 300 million photon particles.

The transport of the injected photons is calculated using the Electron Gamma Shower 5 (EGS5) algorithms [55] in PHITS. With this option, the code calculates not only attenuations of broadband x rays by an x-ray attenuation filter, the object and the IP detector, but also generation and reabsorption of secondary photons and electrons that could be produced via photoelectric effects and Compton scattering in multiplicative cascade processes. In the present simulations, it is found that difference in simulated intensity with the EGS option on and off is minor. Calculated photon and electron sensitivities of the IP with PHITS agree with published results [56,57].

5. Results and discussions

Figure 4 (a) ~ (f) show simulated and experimental x-ray transmission images of the spark plug test object through the CH, Al and brass filters. The transmission images are obtained by dividing a two dimensional intensity image by an intensity value outside the object. Transmitted x rays through the CH and Al filters clearly form the images of the object, but not through the brass filter. Qualitatively, the simulations reproduce the experimental images well. The signal-to-noise ratio is slightly degraded with the Al and significantly worsen with the brass compared to the image observed with the CH. Most parts of the spark plug in the measured image with the brass filter were swamped in background because the transverse dimension of the filter was only slightly larger than the object size, and the IP was exposed to stray x-ray radiation coming around the filter. A high density piece inside the metal body around Y = ~3 cm is

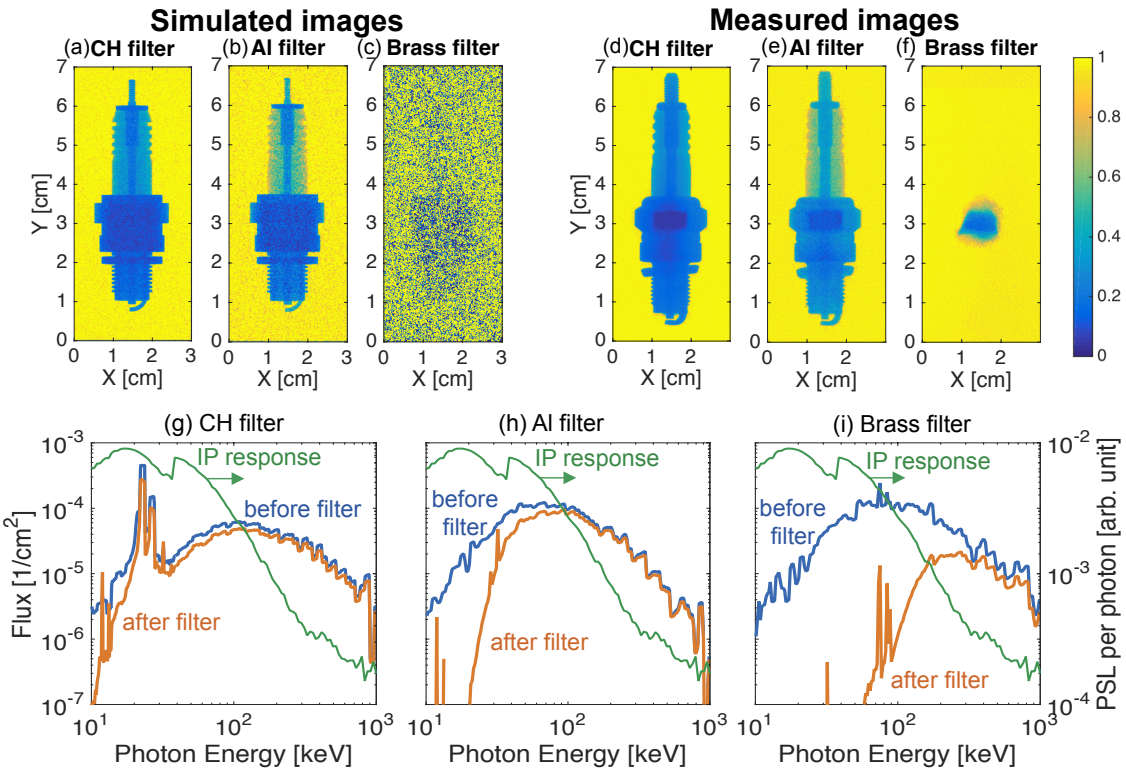

Figure 4 Simulated and experimental radiograph images of the spark plug through (a)(d) CH, (b)(e) Al, and (c)(f) brass filters. Calculated x-ray spectra before and after the filter for (g) CH, (h) Al, and (i) brass. The spectral response of the IP calculated with PHITS is also shown.

not included in the model.

To investigate changes in the shape of the broadband x-ray spectrum due to the attenuation filter and contribution of photon deposition in the IP, Fig. 4(g) ~ (i) compares calculated x-ray spectra entering and exiting the attenuation filters together with the photon sensitivity of the IP detector. The CH filter strongly attenuates photons below 10 keV down to ~1%. This photon cut-off energy (T < 1%) increases to ~ 20 keV and ~100 keV with the Al and brass, respectively. Changing the filter material from low to high atomic number decreases the photon fluxes deposited in the IP's most sensitive range between 10 and 100 keV, resulting in degradation of the image quality. Here, the input x-ray source spectrum for each attenuation filter is the one inferred for the corresponding target type as shown in Table 1 and Fig. 4(g)~(i). The trend of the simulated images is held when using an identical source for all three cases.

Figure 5 compares lineouts of the transmission images for the CH and Al filters. The line profiles are obtained by integrating a boxed area on the insulator of the spark plug from Y=3.8 to 4.9 cm. Three distinct transmission levels identified are an unattenuated intensity by the object (i.e., transmission of 1), the insulating cylinder, and the central rod coupled within the insulating cylinder. The comparisons showing good agreements for both cases further confirms that the input broadband x-ray spectrum characterized by the bremsstrahlung analysis is accurate to reproduce the measured radiographic image. The slight deviation between the experimental and calculated transmission profiles could be due to undisclosed material compositions of the spark plug parts. The experimental and simulated images through the brass filter are evidently too disrupted to obtain valid transmission profiles of the object.

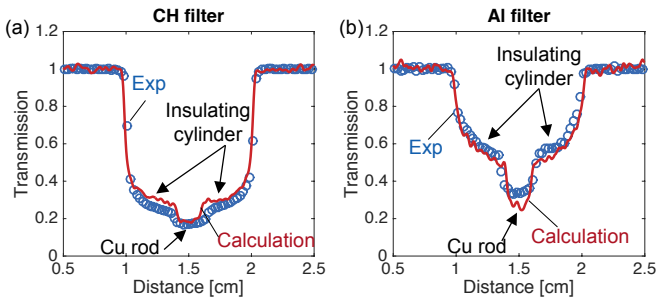

Figure 5 Comparisons of measured and simualted transmission profiles for (a) CH and (b) Al filters.

6. Summary

The experimental benchmarking of laser-driven broadband x-ray radiography using the LSP hybrid PIC and PHITS Monte Carlo codes is presented. The photon transport calculations with PHITS is performed by incorporating the LSP-calculated spectrum, the realistic 3D spark plug model, the x-ray attenuation filter, and the IP detector. This numerical modelling successfully reproduces the experimentally observed radiographic images of a spark plug test object for the three filter materials (CH, Al and brass). In addition, the simulated 1D transmission profiles of a section of the spark plug's insulating cylinder match the experiment well for the CH and Al filters. This result also validates the angular dependent broadband x-ray spectrum inferred from the bremsstrahlung analysis.

While characterization of an x-ray source is necessary for a given short-pulse laser condition, the modelling capability presented here can be used as a predictive tool to design laser-driven broadband x-ray radiography experiments and to optimize details of experimental components such as filter materials, filter thicknesses and detector types without carrying out experiments. The SimpleGeo solid modelar allows ones to design not only a simple symmetric object, but also objects with asymmetric complex structures for photon transport calculations to form radiographic images. This capability is also available with other Monte Carlo software packages such as Geant4 [58] and FLUKA [59]. Furthermore, a broadband spectrum of laser-driven x rays can be readily modified by changing laser and target conditions. With appropriate choices of laser parameters of a PetaWatt class laser and a high sensitivity detector in MeV regimes, the same modelling method could be applied for MeV gamma-ray radiography for industrial applications.

Acknowledgements

The authors would like to acknowledge Dr. P. Wiewior and O. Chalyy for their support of the Leopard laser operations, A. Astanovitskiy, O. Dmitriev, V. Nalajala and V. Davis for conducting the experiment, and the NTF management for allocation of the laser time. H.S. would like to thank Anthony Bass and Brandon Griffin for their help during the experiment. This work was supported by the National Science Foundation under Grant No. 1707357. This collaborative work was partially supported under the auspices of the US Department of Energy by Lawrence Livermore National Laboratory under Contracts No. DE-AC52-07NA27344 and No. DE-FG02-05ER54834 (ACE).

References

[1] Gibbon, P., 2005, Short Pulse Laser Interaction with Matter (Imperial College Press, London)

[2] Herrlin K, Svahn G, Olsson C, Pettersson H, Tillman C, Persson A, Wahlström C G and Svanberg S 1993 *Radiology* 189 65–8

[3] Kieffer J C, Krol A, Jiang Z, Chamberlain C C, Scalzetti E and Ichalalene Z 2002 *Appl. Phys. B* 74 s75–81

[4] Rusby D R, Brenner C M, Armstrong C, Wilson L A, Clarke R, Alejo A, Ahmed H, Butler N M H, Haddock D, Higginson A, McClymont A, Mirfayzi S R, Murphy C, Notley M, Oliver P, Allott R, Hernandez-Gomez C, Kar S, McKenna P and Neely D 2016 *International Society for Optics and Photonics*, p 99920E
[5] Jones C P, Brenner C M, Stitt C A, Armstrong C, Rusby D R, Mirfayzi S R, Wilson L A, Alejo A, Ahmed H, Allott R, Butler N M H, Clarke R J, Haddock D, Hernandez-Gomez C, Higginson A, Murphy C, Notley M, Paraskevoulakos C, Jowsey J, McKenna P, Neely D, Kar S and Scott T B 2016 *J. Hazard. Mater.* 318 694–701
[6] Brenner C M, Mirfayzi S R, Rusby D R, Armstrong C, Alejo A, Wilson L A, Clarke R, Ahmed H, Butler N M H, Haddock D, Higginson A, McClymont A, Murphy C, Notley M, Oliver P, Allott R, Hernandez-Gomez C, Kar S, McKenna P and Neely D 2016 *Plasma Phys. Control. Fusion* 58 014039
[7] Koch J A., Aglitskiy Y, Brown C, Cowan T, Freeman R, Hatchett S, Holland G, Key M, MacKinnon A., Seely J, Snavely R and Stephens R 2003 *Rev. Sci. Instrum.* 74 2130
[8] King J A, Akli K, Snavely R A., Zhang B, Key M H, Chen C D, Chen M, Hatchett S P, Koch J A., MacKinnon A J, Patel P K, Phillips T, Town R P J, Freeman R R, Borghesi M, Romagnani L, Zepf M, Cowan T, Stephens R, Lancaster K L, Murphy C D, Norreys P and Stoeckl C 2005 *Rev. Sci. Instrum.* 76 076102
[9] Theobald W, Solodov A A, Stoeckl C, Anderson K S, Beg F N, Epstein R, Fiksel G, Giraldez E M, Glebov V Y, Habara H, Ivancic S, Jarrott L C, Marshall F J, McKiernan G, McLean H S, Mileham C, Nilson P M, Patel P K, Pérez F, Sangster T C, Santos J J, Sawada H, Shvydky A, Stephens R B and Wei M S 2014 *Nat. Commun*. 5 5785
[10] Sawada H, Fujioka S, Hosoda T, Zhang Z, Arikawa Y, Nagatomo H, Nishimura H, Sunahara A, Theobald W, Patel P K and Beg F N 2016 *J. Phys. Conf. Ser.* 717 012112
[11] Tommasini R, Hatchett S P, Hey D S, Iglesias C, Izumi N, Koch J A., Landen O L, MacKinnon A. J, Sorce C, Delettrez J A., Glebov V Y, Sangster T C and Stoeckl C 2011 *Phys. Plasmas* 18 056309
[12] Tommasini R, Bailey C, Bradley D K, Bowers M, Chen H, Di Nicola J M, Di Nicola P, Gururangan G, Hall G N, Hardy C M, Hargrove D, Hermann M, Hohenberger M, Holder J P, Hsing W, Izumi N, Kalantar D, Khan S, Kroll J, Landen O L, Lawson J, Martinez D, Masters N, Nafziger J R, Nagel S R, Nikroo A, Okui J, Palmer D, Sigurdsson R, Vonhof S, Wallace R J and Zobrist T 2017 *Phys. Plasmas* 24 053104
[13] Sawada H, Daykin T S, Hutchinson T M, Bauer B S, Ivanov V V, Beg F N, Chen H, Williams G J and McLean H S 2019 *Phys. Plasmas* 26 083104
[14] Kemp A J, Fiuza F, Debayle a., Johzaki T, Mori W B, Patel P K, Sentoku Y and Silva L O 2014 *Nucl. Fusion* 54 054002
[15] Robinson A P L, Strozzi D J, Davies J R, Gremillet L, Honrubia J J, Johzaki T, Kingham R J, Sherlock M and Solodov A A 2014 *Nucl. Fusion* 54 054003
[16] Sentoku Y, Paraschiv I, Royle R, Mancini R C and Johzaki T 2014 Phys. Rev. E 90 051102
[17] Chen C D, Kemp A J, Pérez F, Link A, Beg F N, Chawla S, Key M H, McLean H, Morace A, Ping Y, Sorokovikova A, Stephens R B, Streeter M, Westover B and Patel P K 2013 Phys. Plasmas 20 052703
[18] Park H S, Chambers D M, Chung H K, Clarke R J, Eagleton R, Giraldez E, Goldsack T, Heathcote R, Izumi N, Key M H, King J A., Koch J A., Landen O L, Nikroo A, Patel P K, Price D F, Remington B A, Robey H F, Snavely R A., Steinman D A, Stephens R B, Stoeckl C, Storm M, Tabak M, Theobald W, Town R P J, Wickersham J E and Zhang B B 2006 Phys. Plasmas 13 056309
[19] Wilks S C, Kruer W L, Tabak M and Langdon A B 1992 *Phys. Rev. Lett*. **69** 1383–6
[20] Beg F N, Bell A R, Dangor A E, Danson C N, Fews A. P, Glinsky M E, Hammel B A, Lee P, Norreys P A. and Tatarakis M 1997 *Phys. Plasmas* **4** 447
[21] Haines M G, Wei M S, Beg F N and Stephens R B 2009 *Phys. Rev. Lett*. **102** 045008
[22] Courtois C, Edwards R, Compant La Fontaine a., Aedy C, Bazzoli S, Bourgade J L, Gazave J, Lagrange J M, Landoas O, Dain L Le, Mastrosimone D, Pichoff N, Pien G and Stoeckl C 2013 Phys. Plasmas 20 083114
[23] Krol A, Ikhlef A, Kieffer J C, Bassano D A, Chamberlain C C, Jiang Z, Pépin H and Prasad S C 1997 Med. Phys. 24 725–32
[24] Norreys P A, Santala M, Clark E, Zepf M, Watts I, Beg F N, Krushelnick K, Tatarakis M, Dangor A E, Fang X, Graham P, McCanny T, Singhal R P, Ledingham K W D, Creswell A, Sanderson D C W, Magill J, Machacek A, Wark J S, Allott R, Kennedy B and Neely D 1999 Phys. Plasmas 6 2150–6
[25] Schwoerer H, Gibbon P, Düsterer S, Behrens R, Ziener C, Reich C and Sauerbrey R 2001 Phys. Rev. Lett. 86 2317–20
[26] Clarke R J, Neely D, Edwards R D, Wright P N M, Ledingham K W D, Heathcote R, McKenna P, Danson C N, Brummitt P A, Collier J L, Hatton P E, Hawkes S J, Hernandez-Gomez C, Holligan P, Hutchinson M H R, Kidd A K, Lester W J, Neville D R, Norreys P A, Pepler D A, Winstone T B, Wyatt R W W and Wyborn B E 2006 J. Radiol. Prot. 26 277–86
[27] Courtois C, Compant La Fontaine A, Landoas O, Lidove G, Méot V, Morel P, Nuter R, Lefebvre E, Boscheron A, Grenier J, Aléonard M M, Gerbaux M, Gobet F, Hannachi F, Malka G, Scheurer J N and Tarisien M 2009 Phys. Plasmas 16 013105
[28] Mckeever K, Makita M, Nersisyan G, Dzelzainis T, White S, Kettle B, Dromey B, Zepf M, Sarri G, Doria D, Ahmed H, Lewis C L S, Riley D and Robinson A P L 2015 Phys. Rev. E 033107 1–8
[29] Brambrink E, Baton S, Koenig M, Yurchak R, Bidaut N, Albertazzi B, Cross J E, Gregori G, Rigby A, Falize E, Pelka A, Kroll F, Pikuz S, Sakawa Y, Ozaki N, Kuranz C, Manuel M, Li C, Tzeferacos P and Lamb D 2016 High Power Laser Sci. Eng. 4

[30] Armstrong C D, Brenner C M, Zemaityte E, Scott G G, Rusby D R, Liao G, Liu H, Li Y, Zhang Z, Zhang Y, Zhu B, Bradford P, Woolsey N C, Oliveira P, Spindloe C, Wang W, McKenna P and Neely D 2019 Plasma Phys. Control. Fusion 61 034001
[31] Borm B, Khaghani D and Neumayer P 2019 Phys. Plasmas 26 023109
[32] Compant A, Fontaine L, Courtois C, Gobet F, Hannachi F, Marquès J R, Tarisien M, Versteegen M and Bonnet T 2019 Phys. Plasmas 26 113109
[33] Daykin T S, Sawada H, Sentoku Y, Beg F N, Chen H, McLean H S, Link A J, Patel P K and Ping Y 2018 *Phys. Plasmas* 25 123103
[34] Daykin T S, 2019 Ph.D Dissertation, University of Nevada Reno, http://hdl.handle.net/11714/5737
[35] Courtois C, Edwards R, Compant La Fontaine A, Aedy C, Barbotin M, Bazzoli S, Biddle L, Brebion D, Bourgade J L, Drew D, Fox M, Gardner M, Gazave J, Lagrange J M, Landoas O, Le Dain L, Lefebvre E, Mastrosimone D, Pichoff N, Pien G, Ramsay M, Simons A, Sircombe N, Stoeckl C and Thorp K 2011 Phys. Plasmas 18 023101
[36] Clarke R J, Neely D, Blake S, Carroll D C, Green J S, Heathcote R and Notley M 2012 http://doi.org/10.5281/zenodo.1054871
[37] Borm B, Gärtner F, Khaghani D and Neumayer P 2016 Rev. Sci. Instrum. 87 093104
[38] Palaniyappan S, Gautier D C, Tobias B J, Fernandez J C, Mendez J, Burris-Mog T, Huang C K, Favalli A, Hunter J F, Espy M E, Schmidt D W, Nelson R O, Sefkow A, Shimada T and Johnson R P 2019 Laser Part. Beams 502–6
[39] Armstrong C D, Brenner C M, Jones C, Rusby D R, Davidson Z E, Zhang Y, Wragg J, Richards S, Spindloe C, Oliveira P, Notley M, Clarke R, Mirfayzi S R, Kar S, Li Y, Scott T, Mckenna P and Neely D 2019 High Power Laser Sci. Eng.
[40] Welch D, Rose D, Oliver B, and Clark R, *Nucl. Instrum. Methods Phys. Res., Sect. A* 464, 134 (2001)
[41] Sato T, Iwamoto Y, Hashimoto S, Ogawa T, Furuta T, Abe S, Kai T, Tsai P-E, Matsuda N, Iwase H, Shigyo N, Sihver L and Niita K 2018 *J. Nucl. Sci. Technol*. 55 684–90
[42] Theis C., Buchegger K.H., Brugger M., Forkel-Wirth D., Roesler S., Vincke H., 2006, *Nuclear Instruments and Methods in Physics Research A* 562, pp. 827-829
[43] Wiewior P P, Ivanov V V and Chalyy O 2010 *J. Phys. Conf. Ser.* 244 032013
[44] Sawada H, Sentoku Y, Yabuuchi T, Zastrau U, Förster E, Beg F N, Chen H, Kemp A J, McLean H S, Patel P K and Ping Y 2019 *Phys. Rev. Lett.* 122 155002
[45] https://www.sparkplug-crossreference.com/convert/NGK_PN/CR7HSA
[46] Chen C D, King J A, Key M H, Akli K U, Beg F N, Chen H, Freeman R R, Link A, Mackinnon A J, MacPhee A G, Patel P K, Porkolab M, Stephens R B and Van Woerkom L D 2008 *Rev. Sci. Instrum*. 79 10E305
[47] Chen H, Wilks SC, Patel PK, Shepherd R, 2006, *Rev Sci Instrum* 77 10E703
[48] Link A., Freeman R R, Schumacher D W and Van Woerkom L D 2011 *Phys. Plasmas* 18 053107
[49] Sawada H, Sentoku Y, Bass A, Griffin B, Pandit R, Beg F, Chen H, McLean H, Link A J, Patel P K and Ping Y 2015 J. Phys. B At. Mol. Opt. Phys. 48 224008
[50] Quinn M N, Yuan X H, Lin X X, Carroll D C, Tresca O, Gray R J, Coury M, Li C, Li Y T, Brenner C M, Robinson A P L, Neely D, Zielbauer B, Aurand B, Fils J, Kuehl T and McKenna P 2011 *Plasma Phys. Control. Fusion* 53 025007
[51] J. A. Halbleib, R. P. Kensek, G. D. Valdez, S. M. Seltzer, and M. J. Berger, IEEE Trans. Nucl. Sci. 39, 1025 (1992).
[52] Jackson J D 1998 Classical Electrodynamics (New York: Willey) ch 15
[53] M. Sugimoto, M. Konishi, H. Tanabe, and K. Nishikawa, 1996, United States Patent 5565157
[54] Imada S, 2015, United States Patent Application 20160023953
[55] Hirayama H, Namito Y, Bielajew AF, Wilderman SJ and Nelson WR 2005 *SLAC-R-730 and KEK Report 2005-8*. DOI: 10.2172/877459
[56] Meadowcroft A. L, Bentley C D and Stott E N 2008 *Rev. Sci. Instrum.* 79 2–6
[57] Bonnet T, Comet M, Denis-Petit D, Gobet F, Hannachi F, Tarisien M, Versteegen M and Aléonard M M 2013 *Rev. Sci. Instrum.* 84 103510
[58] Agostinelli S, et al., 2003 Nucl. Instruments Methods Phys. Res. Sect. A Accel. Spectrometers, Detect. Assoc. Equip. 506 250–303
[59] Fassò A, Ferrari A, Sala P R and Ranft J 2001 Springer Berlin Heidelberg, pp 955–60